Carbon 200 (2022) 347–360

Contents lists available at ScienceDirect

Carbon

journal homepage: www.elsevier.com/locate/carbon

Carbon fibre lattice strain mapping via microfocus synchrotron X-ray diffraction of a reinforced composite

Jiraphant Srisuriyachot [a,**], Sophie A.M. McNair [a], Yang Chen [a], Thomas Barthelay [a], Rob Gray [a], Jean Bénézech [a], Igor P. Dolbnya [b], Richard Butler [a], Alexander J.G. Lunt [a,*]

[a] Material and Structures Centre, Department of Mechanical Engineering, University of Bath, Bath, BA2 7AY, United Kingdom
[b] Diamond Light Source Ltd, Harwell Science and Innovation Campus, Didcot, OX11 0DE, United Kingdom

ARTICLE INFO

Keywords:
Carbon fibre reinforced polymers
Lattice strain mapping
Fiber orientation
Microstructural characterisation
X-ray diffraction

ABSTRACT

Synchrotron X-ray diffraction (SXRD) strain analysis is well established for high crystalline materials such as metals and ceramics, however, previously it has not been used in Carbon Fibre Reinforced Polymer (CFRP) composites due to their complex turbostratic atomic structure. This paper will present the feasibility of using SXRD for fibre orientation and lattice strain mapping inside CFRPs. In particular, it is the first time that the radial {002} and axial {100} strains of carbon fibre crystal planes have been analysed and cross-validated via numerical multi-scale simulation in a two-scale manner. In order to simplify the analysis and provide comparable estimates, an UniDirectional (UD) CFRP formed into a well-established humpback bridge shape was used. The lattice strain estimates obtained from SXRD showed localised stress concentrations and effectively matched the numerical results obtained by modelling. The mean absolute percentage differences between the two were 25.8% and 28.5% in the radial and axial directions, respectively. Differences between the two measurements are believed to originate from the non-uniform thermal history, forming geometry and tool-part interaction which leads to localised residual strains in the laminate which are unable to be fully captured by the numerical simulation performed. The carbon fibre microstructures of the inner plies adjacent to the tool were found to be significantly influenced by these factors and therefore the largest errors were observed at these locations. The approach presented has significant promise and implications for research into the micromechanics of composite materials and areas for future improvement have been outlined.

1. Introduction

Carbon Fibre Reinforced Polymer (CFRP) composites have become widely used in high-performance structures as they have high specific stiffnesses and strengths which can be tailored for a specific load case. However, the micromechanical behaviour of CFRPs is not yet fully understood due to their heterogeneous interaction which results in complex failure and damage modes. Micro-defects present in the material, such as voids and wrinkles, also have a significant impact on the macroscopic response. These issues limit the ability to fully exploit CFRPs capabilities, and make the design optimisation and validation of such structures challenging. Because of this, the mechanical responses and material properties of this material have been extensively studied in the past few decades. This is especially true for curved aerospace CFRP structures including C-spars and Z-stiffeners in which a through-thickness failure or delamination needs to be carefully considered during part optimisation. Ineffective design of these structures can result in catastrophic failure and the loss of structural integrity [1].

This paper will show the feasibility of using X-ray diffraction (XRD) to investigate the fibre strain of CFRPs, and highlight other potential benefits of this method. In particular, the key benefit of this approach is that localised strain can be computed directly from the changes to the microstructure of the fibres. This can be contrasted with the likes of Digital Volume Correlation (DVC), in which the strain and deformation of the materials at the macro/meso-level are computed/inferred from the geometry changes of the reconstructed computed tomography (CT) of the object under investigation [2,3] relying on the different levels of X-ray absorption of composite constituents. With low-resolution images,

Abbreviations: Finite Element, FE; Representative Volume Element, RVE; Humpback Bridge, HBB.

* Corresponding author.
** Corresponding author.
E-mail addresses: js2580@bath.ac.uk (J. Srisuriyachot), ajgl20@bath.ac.uk (A.J.G. Lunt).

https://doi.org/10.1016/j.carbon.2022.08.041
Received 15 May 2022; Received in revised form 20 July 2022; Accepted 11 August 2022
Available online 26 August 2022

metal particles are generally doped into the CFRP resin to enhance the contrast to achieve the required precision of the DVC [4–6]. Despite this improved contrast, doping is known to alter the composite mechanical properties and structural response [6]. Even in the case of low contrast in the composite materials, the XRD method does not require the use of doping particles which means that the CFRP is fully representative of samples used in practice. As a result, diffraction can provide a direct measure of strain within the fibres at the microscopic level. The outcomes of this method can also be used alongside existing imaging methods to provide supplementary information into the material behaviour at different length scales. It should therefore be understood that this method does not intend to replace the existing non-destructive testing (NDT) techniques such as CT and C-scan, but to offer new/-complementary information into load distribution and the associated impact of localised defects within the materials which cannot be quantified in the same way using these methods. The key motivation of this study is therefore to ascertain if careful analysis of the XRD patterns of CFRPs can be used to quantify fibre strain within a representative, undoped sample. Whilst the implications and potential applications of this type of measure are broad, it is not intended to replace existing imaging methods, but to offer new information that is essential to enhance existing understanding of load redistribution inside CFRP samples.

XRD works on the principle of Bragg's law which states that an X-ray incident on a crystal surface with an angle of θ will be scattered at the same angle, θ. The scattered wave is sensitive to the lattice spacing between atoms in the fibre and can be either in-phase or out of phase, which results in either a diffraction pattern or no pattern forming on the detector. In this way, the positions and shapes of the peaks can be used to gain insight into the lattice structure and micromechanical response of the materials.

XRD has previously been used to determine the degree of crystallisation and crystal sizes of commercial, high-performance carbon fibres at different grades. Fibre interplanar d-spacing (d_{002}) has been shown to be influential on the elastic modulus. Different fibres are also known to have different degrees of crystallisation depending on the fabrication route [7], heat-treatment process [8,9] as well as the type of precursor [10]. Additional heat treatment results in the alignment of graphite planes with the fibre axis and an increase in crystallisation which results in a higher fibre elastic modulus [9,11]. The most common precursor for the high-performance carbon fibres is Polyacrylonitrile (PAN) [12], for which the degree of crystallisation ranges between 65% and 83% [9]. To investigate the microstructure of this type of carbon fibre, Johnson [13] employed wide-angle XRD and small-angle XRD. This analysis showed that the fibres have no regular three-dimensional order, needle-shaped voids exist between the graphite planes at the outer surface, and the planes were folded extensively at the core. In short, this analysis revealed that the crystal size and the arrangement of the graphite gradually decrease from the surface to the core.

Changes to lattice strains from residual effects such as thermal expansion and those generated by in-situ loading are now well established for highly crystalline structures such as metals and ceramics [14–17]. However, XRD has not been widely used to study strain distribution in CFRP composite laminates due to the complex interplay between crystalline carbon (graphite) and semi-crystalline carbon (turbostratic) in the fibres, and the amorphous structure of the polymer matrix. In particular, the diffraction of the semi-crystalline and amorphous structures reduces peak intensity and broadens the diffraction peak, when compared to the crystalline response. For this reason, only a limited number of XRD in-situ loading studies determining lattice strain directly from the carbon fibre have been conducted. Nishino et al. facilitated XRD to investigate the effect of environmental conditions on stress transfer in transversely loaded CFRPs [18,19]. Within this study, the {004} diffraction peak was characterised in preference to {002} peak as the larger scattering angle is less affected by the amorphous halo [18]. However, the peak intensity of {004} was found to be overwhelmed by the {002} peak, meaning that effective strains measurement could not be achieved.

Lab-based XRD experiments are limited by poor peak resolutions, large gauge volumes, high noise as well as a long acquisition times. In contrast, synchrotron radiation facilities can provide a much higher flux intensity and can be precisely focused/collimated, resulting in higher resolution and shorter acquisition times. In this experiment, Synchrotron X-ray diffraction (SXRD) was used to study the through-thickness properties of Humpback Bridge (HBB) CFRPs during in-situ compressive loading. This geometry was developed by Wisnom et al. [20], as under pure bending, a single or double curvature induces radial stress only, whereas the HBB geometry leads to impure bending which generates interlaminar shear stresses [21]. As a consequence, the combination of radial and shear stresses can lead to out-of-plane delamination which has important implications for the reliable use of CFRPs [22,23]. It should be noted that numerous studies have attempted to determine the through-thickness properties experimentally [21,24–26], as well as using numerical simulations in order to predict the delamination failure [27,28]. However, the resolutions and reliability of these approaches mean that significant uncertainty remains.

Therefore the main goals of this study are to enhance the current understanding of delamination failure whilst simultaneously showing the feasibility of the XRD method to determine the fibre orientations and strain distributions in composite materials. This analysis is based on using the HBB sample [20] to gain a better understanding of the correlation of material behaviour and its geometry. In order to validate this new approach, complementary numerical multi-scale modelling in two-scale approach between meso- and micro-scale has also been performed. Both qualitative and quantitative results will be discussed.

2. Methodology

2.1. Sample preparation

The test specimen was manufactured from 16 layers of Unidirectional (UD) AS4/8852 prepreg with a nominal thickness of 3 mm. The sample was laid upon an aluminium mould to form the HBB shape with a nominal outer dimension of 180 × 100 mm^2. The sample was debulked every three plies during the lay-up process. It was then cured in an autoclave under temperature 110 °C for 30 min before being increased to 180 °C and held for 2 h under pressure at 7 bar, with an approximately −0.2 bar vacuum pressure. The sample was then cooled down to the ambient temperature, 20 °C, at the rate of 5 °C/min, as recommended by the manufacturer. Subsequently, strips of 3 mm width and 50 mm length were cut off using a diamond wire saw as shown in Fig. 1.

2.2. Experimental setup

In-situ tests were performed on the B16 beamline at Diamond Light Source, UK. A monochromatic beam energy of 19 keV (wavelength = 0.65 Å) was selected using the Double Multilayer Monochromator and a focused beam spot size of 10 × 10 μm^2 was achieved using Compound Reflective Lenses (CRLs, 98 Beryllium lenses in total, parabolic, radius of curvature in apex R = 200 μm). A Photonic Science Image-Star 9000 large-area X-ray detector with a sensor size of 3056 × 3056 pixels and an effective pixel size of ~31 μm was employed to collect the XRD patterns. As a compromise between the quality of the data and the number of points scanned, an exposure time of 5 s was selected. Lanthanum Hexaboride (LaB_6) was used as a calibrant to determine the sample-to-detector distance (109.14 mm), beam centre and detector geometrical distortion correction.

A Deben CT5000 5 kN load cell, co-axially fixed onto a tomography tower, was used to perform in-situ compressive testing of the specimen. The tower was composed of an Aerotech goniometer, along with multiple Huber and Newport motorised angular and translational stages, to facilitate the sample alignment required for SXRD and Synchrotron

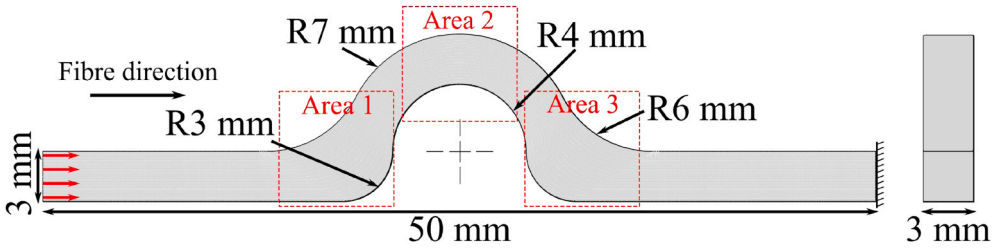

Fig. 1. Dimensions of 16 ply UD HBB sample; the SXRD and SCT scanning areas are highlighted in red boxes. The direction of distributed load is represented by red arrows, and the sample is fully fixed on the right. (A colour version of this figure can be viewed online.)

Computed Tomography (SCT) to be performed at the location of interest. For the SXRD, the sample was rastered across the focused beam to form a grid array row-by-row. The distances between each measurement point were set to be 100 μm horizontally and 500 μm vertically to provide the high-resolution insights required to capture the localised effects. Between each scan, a compressive load was applied at a rate of 0.1 mm/min along the primary fibre axis of the HBB. An in-house grip was manufactured from steel with geometry as shown in Fig. 2a to hold the sample under compression. Data collection was performed at 350 N and at the first breaking load, approximately 530 N on average. Mapping was performed at each load increment at three different areas as shown in Fig. 1, where the maximum interlaminar shear stress and failures are expected to take place.

At each load increment, SCT was also performed at the same location. To facilitate this analysis the CRLs were removed, and a PCO.edge high-speed 5.5 X-ray camera was used to capture radiographs while the sample was being rotated. This detector field of view was $3.2 \times 3.8\ mm^2$ with an effective pixel size of 3 μm and data was collected over 180° rotation with an increment of 0.2° (900 projections) and an exposure time of 0.5 s. A flywheel scan was used to reduce the total scanning time to produce 2160 cross-sectional images at a resolution of 2560 × 2560 pixels. A schematic representation of the experimental setup is shown in Fig. 2b.

Following the experiment, five nominally identical samples were loaded to failure using the Deben load cell. This study was used to compare the failure modes and stiffness of the group to gain insight into the representative nature of the sample and the statistical difference between nominally identical samples.

2.3. Synchrotron X-ray diffraction analysis

A conventional ConFit (conversion + fitting) method [29] was implemented to analyse the SXRD data in three main steps: calibration, data reduction from 2D patterns into 1D intensity vs scattering angle, and peak centre fitting.

The Data Analysis Workbench or DAWN [30] developed by Diamond Light Source was used for data reduction in this experiment. The SXRD image was segmented into small azimuthal sections, often referred to as 'caking', before being azimuthally integrated into an intensity vs scattering angle. The azimuthal angle was measured clockwise starting from the equator line (3 o'clock) in the SXRD pattern as shown in Fig. 3. A 4° azimuthal angle interval (total of 90 azimuthal bins) was used as a balance between peak intensity and azimuthal resolution. To restrict the processing area and exclude noise data from the loading cell casing

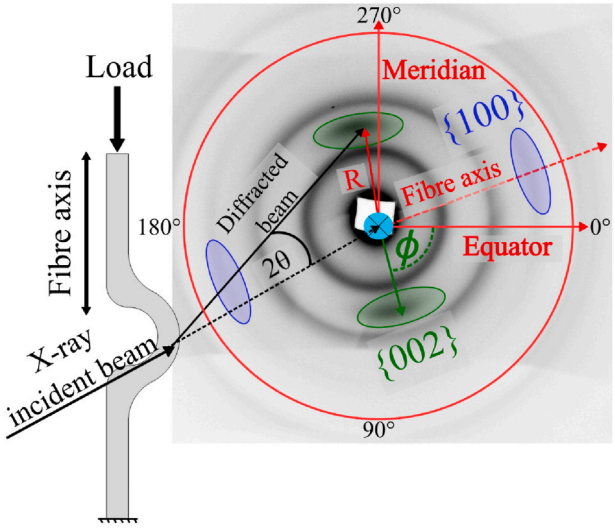

Fig. 3. Example of the SXRD diffraction pattern; the principal diffraction features arising from the carbon fibre structure {002} and {100} are highlighted in green and blue, respectively; the nominal meridian and equatorial axes are shown along with an outer bound of the processing region; R is the radial distance from the beam centre to the diffraction peak; θ is Bragg angle, and φ is the azimuthal angle of the scattered beam. (A colour version of this figure can be viewed online.)

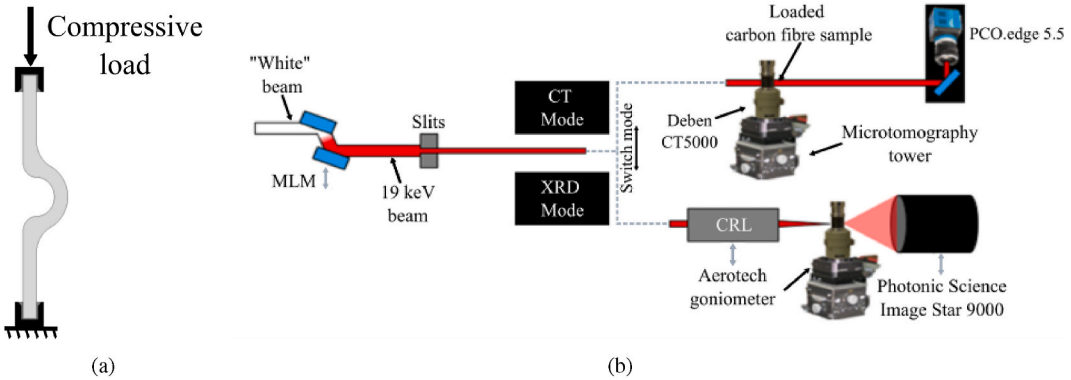

Fig. 2. (a) Mechanical loading configuration along with an in-house grip geometry. (b) Schematic of SXRD and SCT beamline setup at B16, Diamond Light Source, UK; At each load increment, the modes were switched to facilitate both SXRD and SCT. (A colour version of this figure can be viewed online.)

shadow, 1350 radial bins were used.

Two different integration profiles, 'radial' and 'azimuthal' integration, were obtained from the data reduction process in order to determine the fibre orientation and the lattice strains, respectively. The principal difference between these two approaches is that radial integration is the average intensity in each radial bin plotted against the azimuthal angle, whereas azimuthal integration is an averaged intensity of the specified azimuthal bins plotted against radial distance. The final steps of the ConFit method are to remove the background (a linear fit was found to be suitable) and then determine the positions of the peak centres. A Gaussian function was found to provide a reasonable localised fit to the diffraction peaks and was therefore used to quantify the peak centres. Fig. 3 depicts the two main features of the diffraction pattern. The green and blue ovals highlight the diffraction peak positions where the Bragg condition was met. In particular, they represent {002} interplanar plane diffraction and {100} in-plane diffraction of the basal plane, respectively. The full bright rings shown in the diffraction image arise from the diffraction of the loadcell's glassy support tube, which had to be omitted or subtracted from the diffraction profile. In the subsequent analysis of the lattice d-spacing in the particular direction will be denoted by the standard notation d_{hkl}. Importantly it should be noted that the lattice strains of the interplanar {002} and in-plane {100} correspond to the radial and axial strains of the fibre, allowing effective comparisons to be drawn with the modelling simulation performed.

2.4. Finite Element analysis

2.4.1. Meso-scale model

In order to predict the mechanical response and failure of a composite laminate, a three-dimensional Finite Element (FE) model of the HBB was developed using ABAQUS software based on a cohesive damage model to account for delamination [31]. However, the main objective of this static analysis is to provide numerical validation to the SXRD lattice strain determination before the failure in the elastic regime. A clamped boundary condition was applied to both ends of the sample, and a mechanical compressive loading was applied at one end. The HBB was made of 16 layers of UD AS4/8552 prepreg with a nominal thickness of 3 mm. The material properties of the AS4/8552 prepreg and interface are stated in Table 1. The material orientation was assigned with respect to the HBB geometry.

Each fibrous layer was modelled with the eight-node brick element (C3D8R-Enh) assuming a ply thickness of 172.5 μm. This element type was chosen to account for tri-axial stresses and to prevent shear locking which can be a source of underprediction of bending stiffness [33]. The global element size of the model was selected to be equivalent to the nominal ply thickness with five elements used per ply thickness in order to optimise run time whilst simultaneously having sufficient fidelity to capture the main effects. Cohesive elements (COH3D8), available in ABAQUS, were inserted between the plies with 15 μm thickness [34] to represent delamination damage under a traction-separation law with mixed-mode fracture energy.

Table 1
HexPly AS4/8552 UD prepreg CFRP material properties used as inputs for meso-scale modelling [32]. E_{11} is longitudinal modulus, E_{22} is transverse modulus, G is shear modulus, ν is Poisson's ratio, α is coefficient of thermal expansion, N^c is normal strength, S^c is shear strength, G_{IC} is Mode I critical energy release rate, G_{IIC} is Mode II critical energy release rate, η_{BK} is BK exponent specifically to this material.

Property		
Ply elastic properties		
E_{11}	134	GPa
$E_{22} = E_{33}$	8.8	GPa
$G_{12} = G_{13}$	4.9	GPa
$\nu_{12} = \nu_{13}$	0.314	
ν_{23}	0.487	
Ply thermal expansion coefficient		
α_1	0.21×10^{-6}	/C°
α_2	3.3×10^{-5}	/C°
Interface properties		
N^C	74	MPa
S^C	110	MPa
G_{IC}	0.30	kJ/m^2
G_{IIC}	0.87	kJ/m^2
η_{BK}	1.45	

The traction-separation law consists of three different regimes: initial linear elastic behaviour, damage initiation criterion, and damage evolution law with mixed-mode response as shown in Fig. 4. The following quadratic nominal stress criterion, Equation (1), was used to predict the onset of delamination in this study.

$$\left\{\frac{\langle t_n \rangle}{N^C}\right\}^2 + \left\{\frac{t_s}{S^C}\right\}^2 + \left\{\frac{t_t}{S^C}\right\}^2 = 1 \tag{1}$$

where t_n, t_s, t_t represent nominal traction stress vector under the deformation is either purely normal to the interface or purely in the first or the second shear direction, respectively. According to literature [35–38], this criterion can predict the location of the delamination reasonably accurately.

Once the damage initiation criterion is met, the cohesive layers start to incur damage, and their material stiffness are degraded linearly assuming linear softening, as defined in Equation (2).

$$D = \frac{\delta_m^f\left(\delta_m^{max} - \delta_m^0\right)}{\delta_m^{max}\left(\delta_m^f - \delta_m^0\right)} \tag{2}$$

where a scalar damage variable, D, represents the overall damage in the cohesive layers. D develops monotonically from 0 to 1 upon further loading after damage initiation. δ_m^f is the effective displacement at complete failure, δ_m^0 is the effective displacement at the initiation of damage, and δ_m^{max} is the maximum value of the effective displacement attained during the loading history. The material softening stress components can be accommodated using the following equations:

$$\begin{aligned} t_n &= \begin{cases} (1-D)\overline{t_n}, & \overline{t_n} \geq 0 \\ \overline{t_n}, & \overline{t_n} < 0; \end{cases} \\ t_s &= (1-D)\overline{t_s}; \\ t_t &= (1-D)\overline{t_t}. \end{aligned} \tag{3}$$

where $\overline{t_n}, \overline{t_s}, \overline{t_t}$ are the stress components predicted by the elastic traction-separation behaviour for the current strains without damage. The delamination process in composite material is frequently driven by mixed-mode fracture in which the damage could potentially start propagating before one of the maximum traction stresses is achieved, as

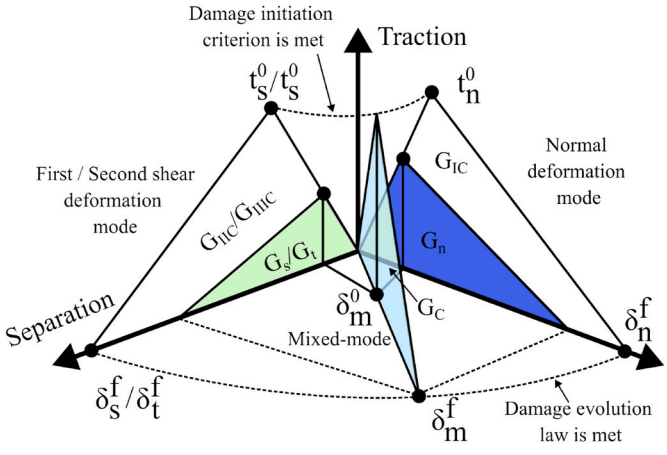

Fig. 4. Typical bilinear constitutive traction-separation response of cohesive layers under mixed-mode fracture energy.

can be seen in Fig. 4. The dissipated fracture energy resulting from damage is equivalent to the area under the curve. Benzeggagh-Kenane (BK) [39] proposed the damage evolution criterion of the cohesive layers based on mixed-mode energy as:

$$G_{IC} + (G_{IIC} - G_{IC})\left\{\frac{G_S}{G_T}\right\}^{\eta_{BK}} = G_C; \quad \text{where} \quad G_S = G_s + G_t, G_T = G_n + G_S \tag{4}$$

and $G_C = G_n + G_s + G_t$. This equation was used to capture the mixed-mode response observed in this study.

The influence of thermal residual strain from cooling during the curing process was simulated from a predefined field thermal analysis (in advance of the compressive loading). A simple cooling process from stress-free temperature to room temperature using a constant coefficient of thermal expansion (CTE) would lead to the overestimation of residual strain in the laminate as it does not account for the attenuating influence parameters such as humidity and moisture ingression. To provide a better estimate of the true residual strain, a half temperature drop from the stress-free temperature at 180° for resin 8552 to the room temperature 20° was applied, as has widely been used within the literature [32, 40].

2.4.2. Micro-scale modelling

A linear constitutive Representative Volume Element (RVE) model of a carbon fibre composite at the micro-scale was implemented alongside the meso-scale simulation in the Top-Down approach manner, in order to capture the behaviour of carbon fibres individually and simplify the modelling. A 50-μm cubic RVE with 57% fibre volume fraction of (38 fibres) randomly distributed parallel fibres was generated to compute the average fibre strains and compare them with the SXRD lattice strain mapping. The RVE was created using the fibre propagation method developed by Yang et al. [41] to achieve a high fibre volume fraction with a constant fibre diameter of 7 μm. The fibre and matrix phases were considered to be anisotropic and isotropic materials at this scale, respectively as used by Refs. [42,43]. The material properties of both phases are stated in Table 2. These properties at the micro-scale are corresponding to the ply properties under the rule of mixture.

The through-thickness strains obtained from the meso-scale model were extracted with a dedicated python script and subsequently used as the loading conditions of the RVE simulations to determine the fibres strain. The AMITEX_FFTP solver that uses the Fast Fourier Transforms (FFTs) [45, 46] was used for this analysis, where periodic boundary conditions were naturally applied. The RVE strain tensors were computed in the Cartesian coordinate system which needed to be transformed into the Cylindrical coordinate system to compare with the 2D SXRD fibre lattice strains in the radial and axial directions. A schematic overview of the interaction between the meso- and microscopic simulations is illustrated in Fig. 5. The strains in the matrix were not considered in detail in this study as the diffraction patterns are too diffuse to reliably assess this material. The output notation from this analysis was the average radial and axial strains of the fibre.

Table 2
Mechanical properties of AS4 carbon fibre and 8552 epoxy resin matrix used in the RVE modelling [43,44].

Property		
AS4 carbon fibre		
E^f_{11}	231	GPa
E^f_{22}	13	GPa
G^f_{12}	11	GPa
ν^f_{12}	0.30	
ν^f_{23}	0.46	
8552 epoxy resin		
E^m	5.07	GPa
ν^m	0.35	

3. Results and discussion

3.1. X-ray diffraction data analysis and interpretation

Peak intensity thresholding of the diffraction patterns was used to determine whether the incident X-ray was on-sample or off-sample, to identify sample edges and the location of delamination as well as the presence of resin-rich zone. When the incident X-ray is on-sample, unique diffraction contours were formed on the XRD image as shown in Fig. 6a. The image was then integrated azimuthally into radial profiles at the 2-theta angles corresponding to the {002} and {100} peaks in order to determine the orientation of the crystal planes. As expected the results showed that the {002} peaks (green) were 90° offset to the fibre axis, and two distinct diffraction peaks of {100} (blue) were present due to the hexagonal shape of the basal planes around the fibres. It should be noted that one of these two peaks was found to have an intensity greater than the other, due to low-level shadowing from the experimental setup. The predominant peak was labelled as {100} which was oriented in the same direction as the fibre axis.

Once the fibre orientation is known, azimuthal integration in that direction can be used to determine the Bragg angle of the crystal planes. It is essential to limit the integration angle range and locate the fibre orientation in order to separate the {100} and $\{100^*\}$ peaks as the lower intensity peak could shift the peak centre from the full azimuthal integration operation. It should be noted that the diffraction peaks matched those previously identified within the literature both in terms of scattering angle and relative intensities [7]. The peak intensity of {100} was determined to be half intensity of the {002}, and approximately the same magnitude as the amorphous halo from the load cell. Previous studies have shown that the peak intensity of the {100} reflection can be increased by performing diffraction at the end face of carbon fibres or in a direction parallel to the longitudinal fibre axis [7]. However, the geometry of the HBB means that neither of these approaches is geometrically possible for a unidirectional layup.

In order to understand how the strain orientations within the fibre correspond to the lattice strain measured, careful consideration of the structure of the fibres is required. The PAN-based carbon fibre model proposed by Johnson [13] shown in Fig. 6b, was found to effectively match the diffraction patterns and lattice strains identified. Within this model the basal plane stacks radially on the outer surface of the fibre such that the change in d-spacing of {002} corresponds to 'radial strain'. The stacking orientation is typically referred to as the 'c-axis' within graphite. The broadening of the diffraction peak which can be seen in the {002} plane is caused by the bending and twisting of the turbostratic structure at the core [49]. In contrast to the above, the primary {100} peak is aligned with the fibre axis such that the change in d-spacing in this orientation can be considered to be 'axial strain'. The same manner was found by Qian et al. [50]. It should be noted that the change in d-spacing in $\{100^*\}$ at an angle 90° offset from the main peak represent the 'circumferential strain', however, the peak intensity of this data was found to be insufficient to perform the reliable fitting. For this reason, circumferential analysis was not explored further.

3.1.1. Fibre orientation determination

In order to map the fibre orientation within the sample, radial integration analysis was repeated for each diffraction pattern to determine the {002} peak centre in term of azimuthal angle (φ), as shown in Fig. 6a. The angle of the {002} fitting was found relative to the equator axis ($\varphi = 0°$). As expected the location of the diffraction peak rotated in accordance with the sample curvature. It should be noted that the {002} peak is produced by constructive X-ray interference from the stacked graphene layers within the fibres as described above. As a result, the diffraction angle is always 90° offset to the fibre axis, (fibre angle = 90°

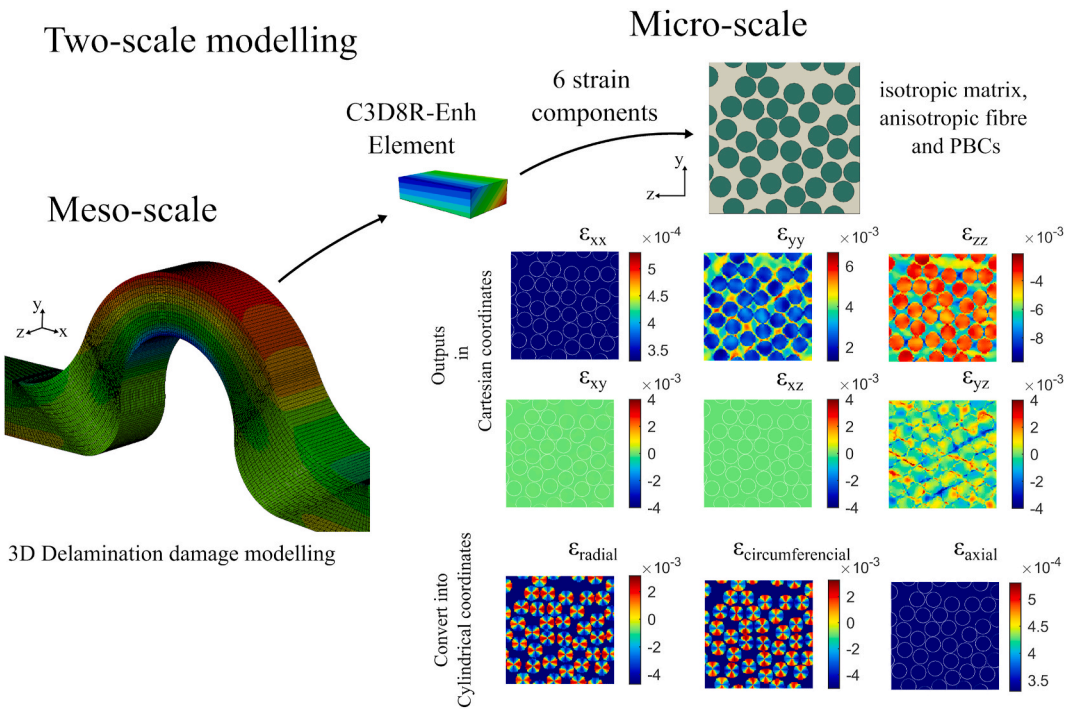

Fig. 5. Schematic diagram of two-scale modelling. A 3D HBB model was developed to predict delamination. Six strain tensors were extracted from each individual element at its integration points and were used as input strains for the micro-scale modelling. An RVE with randomly distributed fibres was used to represent the micro-scale model, in which the isotropic matrix and anisotropic fibres properties were simulated. Periodic Boundary Conditions (PBCs) were applied to the RVE corresponding to the input strain from each direction. The fibre strain was extracted in cartesian coordinates and converted into cylindrical coordinates in order to compare with SXRD results. A typical RVE result computed from a single element of the meso-scale modelling is shown. (A colour version of this figure can be viewed online.)

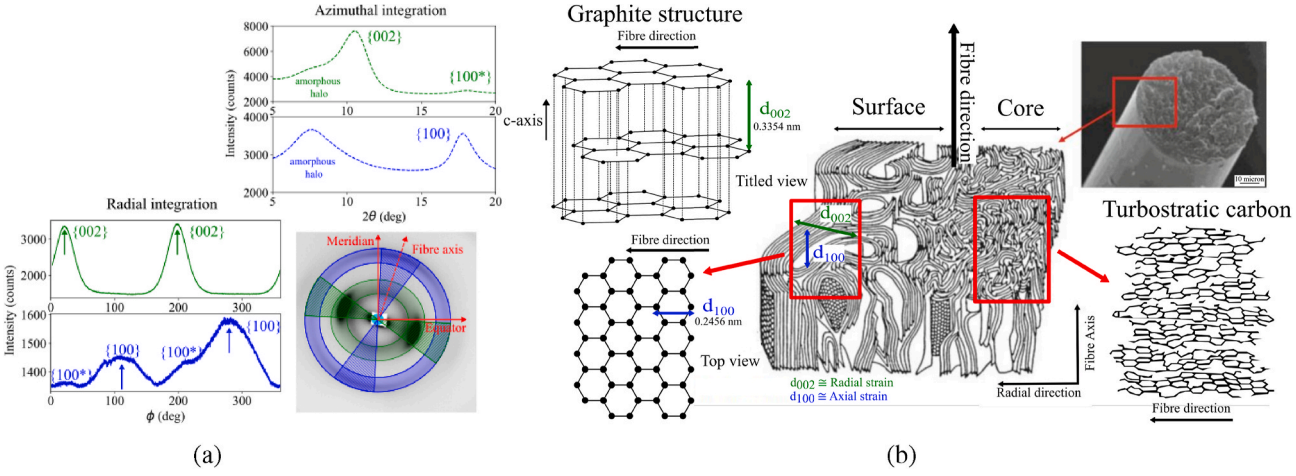

Fig. 6. Schematic of SXRD and associated microstructure of carbon fibre. (a) Diffraction pattern arising from X-ray interaction with the fibres in a direction perpendicular to the fibre axis. The inner Bragg peak (solid green) represents the diffraction between the graphene layers, {002}, and the outer Bragg peak (solid blue) represents the diffraction of the in-plane carbon atoms, {100}. Radial integration of both peaks reveals the rotation of the graphite structure in respect to the meridian/equatorial directions (φ). Azimuthal integration at the primary Bragg peaks orientation as a function of 2θ from the beam centre was performed in directions parallel and perpendicular to the fibre axis. (b) Microstructures of a PAN-based carbon fibre showing the graphite layers that are parallel and aligned at the surface, but have random orientation/alignment in the turbostratic core (modified from Refs. [47,48]). As a result the graphite layers are stacked in the radial direction and the change in interplanar $d_{\{002\}}$ d-spacing is a measure of the fibre radial strain. In contrast the preferred orientation of the d-spacing $d_{\{100\}}$ was observed in a direction parallel to the fibre axis such that it provides a measure of fibre axial strain. (A colour version of this figure can be viewed online.)

$-\varphi$). It is possible to map the orientation from the {100} peak which corresponds to the fibre axis angle; however, he peak intensity is reduced and asymmetric which leads to a higher uncertainty in curve fitting. Therefore, the {002} peak was preferable in this case. The fibre orientation determination in the HBB from the collected data is shown in Fig. 7 which is subsequently used to determine the Bragg angle. It should be noted that this analysis provides the average orientation of the fibres through the full 3 mm width of the sample.

It was found that there is a significant drop in the diffraction image intensity around the sample where there was no/insufficient diffraction of the fibres. Threshold intensities were set to classify the data into three categories such as 'On fibre', 'Off-fibre' and 'Resin rich'. The {002}

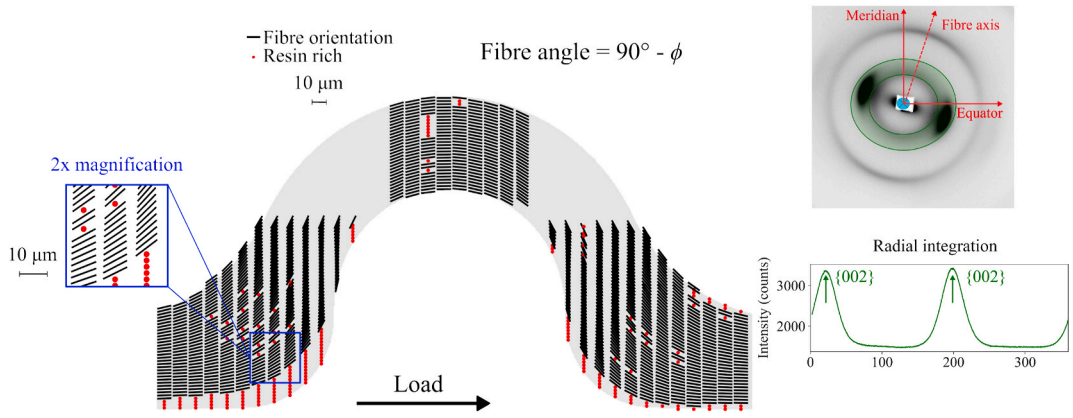

Fig. 7. Grid plot of HBB fibre orientation determined via SXRD. The example data set shown is under a 350 N load, although nominally identical distributions were observed at each load. Within the figure, the orientation is shown by the angle of the black line, red spots being the points where reliable estimates could not be obtained (resin rich points). Each point is an average fibre angle through thickness over the 10 μm beam diameter. An example of SXRD radial integration at the {002} peak is also shown. The fibre angle can then be determined by applying a 90° offset to the azimuthal angle (φ) of the fitted {002} peak centre. (A colour version of this figure can be viewed online.)

peaks completely disappeared in the off-fibre position and were therefore not analysed further or plotted in the figure. Furthermore, the resin rich points (indicated by red dots) gave a high uncertainty in fitting the peak centres which also presented difficulties for further analysis. A significant amount of resin rich points represented at the inner plies around the transition radii, along with a few distributed at other locations within the sample. These points were found to represent voids or damage. However, it did not present in the SCT image at the particular load. This resin rich zone had been confirmed with the tomography image as shown in Fig. 8.

3.1.2. Lattice strain determination

Bragg's law can convert the scattering angle (θ) to the average lattice/d-spacing of the fibre within the gauge volume. In order to perform this calculation Equation (5) can be used where the D-spacing (d) is the average atomic lattice spacing and (λ) is the wavelength of the incident X-rays (at 19 keV, $\lambda = 0.65$ Å).

$$d = \frac{\lambda}{2\sin\theta} \tag{5}$$

The diffraction pattern maps collected at different increment loads facilitated the quantification of changes in the crystalline structure of carbon fibres. In particular, the change in d-spacing (d_{hkl}) with respect to the unstrained d-spacing (d^0_{hkl}) can be used to determine the strains (ε_{hkl})

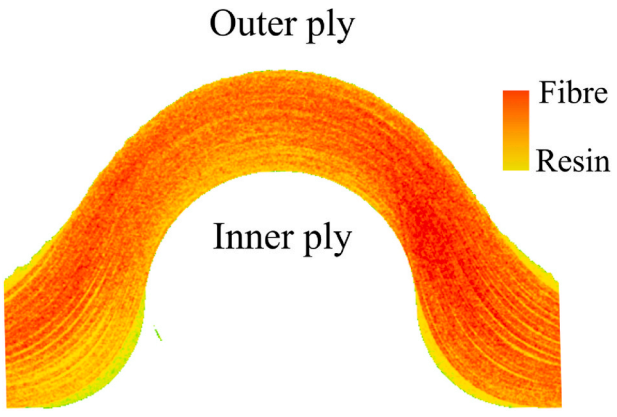

Fig. 8. X-ray computed tomography image of the HBB sample after grayscale image segmentation. Fibre volume fraction can be visualised across the sample. Resin rich regions were observed at the transition corners and varied through-thickness. (A colour version of this figure can be viewed online.)

via Equation (6). The changes in d_{002} and d_{100} are equivalent to the 'radial' and 'axial' strains of the fibres. It is worth noting that these lattice strains are associated with average changes to the graphitic structure through the 3 mm through-sample gauge volume in the same way as the fibre orientation determination. The regular atomic arrangement and constructive interference generated within these regions also mean that this structure dominates the diffraction response. In contrast, the turbostratic nature of the carbon within the centre of the fibres reduces the diffraction response to produce a more diffuse peak that primarily influences the width of the diffraction peak, rather than the peak centre.

$$\varepsilon_{hkl} = \frac{d_{hkl} - d^0_{hkl}}{d^0_{hkl}}; \tag{6}$$

The raster scanning used to generate diffraction maps meant that the shadow shape changed from one position to another, thereby preventing the use of a uniform mask in the post-processing data reduction. As a result, shadowing of the load cell prevented successful peak fitting to be performed at a few nominal points which are shown as black in Fig. 9. Shadowing was found to be particularly problematic for the quantification of the d^0_{100} peak at the top of the sample which resulted in multiple error points and a shifting of the peak centre in the radial map. In order to determine the unstrained lattice parameter, diffraction patterns of an uncured UD prepreg were collected during the experiment to give estimates of $d^0_{002} = 3.480520$ Å and $d^0_{100} = 1.960824$ Å. The d^0_{002} estimate was found to fall well within the literature values for PAN-based carbon fibres of 3.46 Å and 3.66 Å [7,50,51]. Comparisons with literature values for the d^0_{100} were more problematic as only one reference paper of a PAN-based fibre has been reported, which found this value to be between 2.22735 Å and 2.2748 Å [50]. Despite this, the distribution of strain observed was found to be realistic in terms of magnitude and variation, and compared well with numerical FE predictions, such that there was confidence in this estimate.

Fig. 9a and b shows the development of lattice strain before and after failure. During loading, the HBB sample is subjected to an impure bending load, which results in a gradual strain change from compression to tension from the inner to outer plies across the centre part as shown in Fig. 9b. This is in line with the beam bending theory and previous studies of a double curvature structure subjected to end loading [24], and four-point bending test [28]. The locations of strain concentration were revealed around the transition corners which could be a cause of failure. After failure, strain is relieved in the delaminated plies, and a load/strain increase was observed in the bulk.

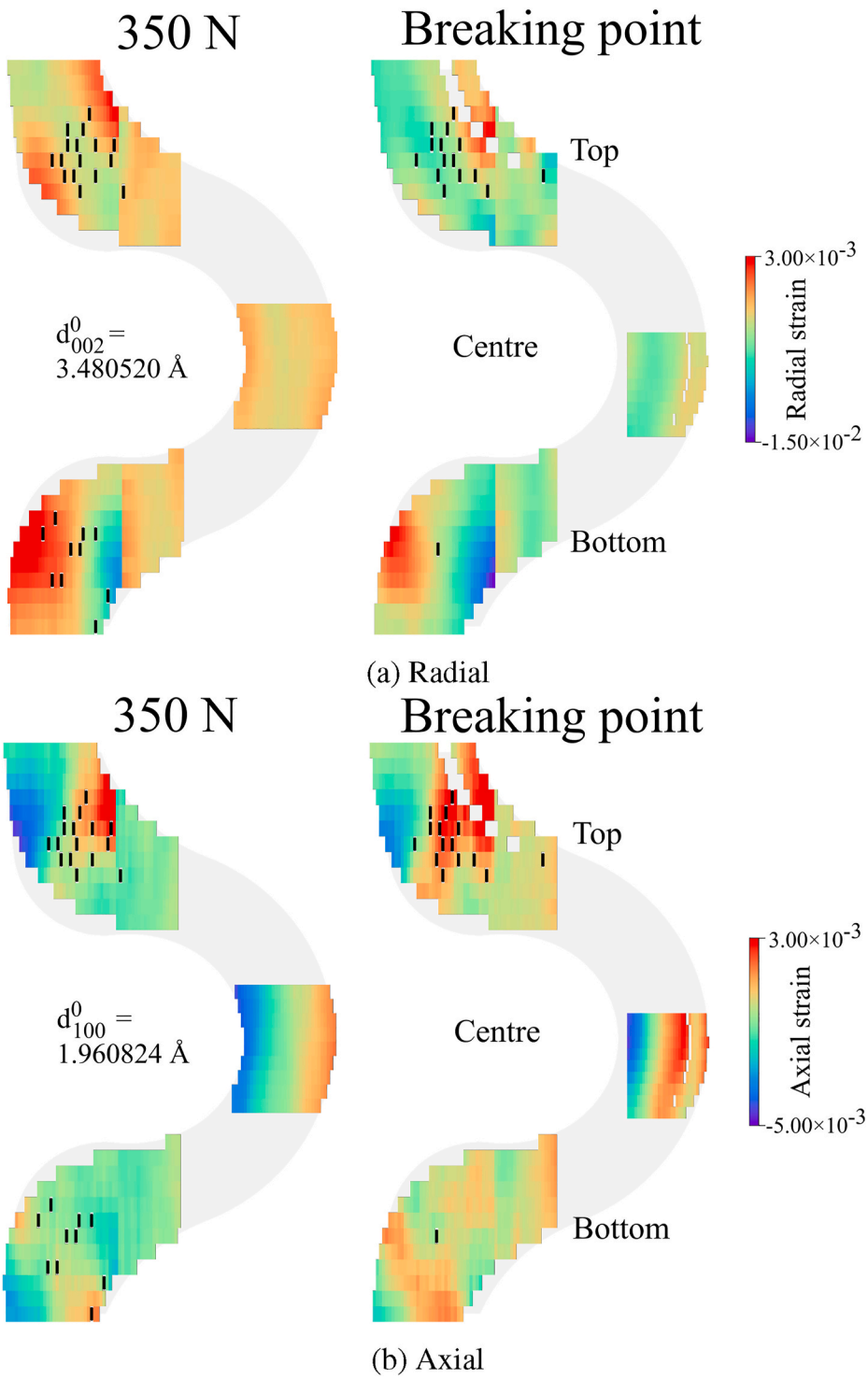

Fig. 9. (a) radial and (b) axial lattice strains within the fibre at 350 N and following breakage at 530 N. Erroneous points are marked in black. (A colour version of this figure can be viewed online.)

The SCT in Fig. 10 shows that the failure occurred near the outer plies halfway through the middle ply at the top/centre part of the specimen. It was found that delamination was initiated between the plies in the presence of intralaminar cracks running across the sample width. This suggests that the interfaces between the non-uniform distributed fibres and matrix were weaker than the resin rich zone between each ply. It is possible that matrix cracking induced high stress concentrations which triggered the delamination via a mixed mode fracture however it was not possible to locate the exact origin of the crack as it propagated suddenly. The main focus of this study was to identify if SXRD can resolve the load redistribution occurring after sample failure, rather than focusing on damage evolution. Accordingly, very few load increments could be achieved within the beamtime awarded. Fortunately, however, the method provided has been shown to be viable to study this type of effect. Therefore, by using smaller load increments in future, the evolution of failure could theoretically be monitored in-situ in order to determine how failure propagated.

It should be noted that there is an absence of data at the inner and

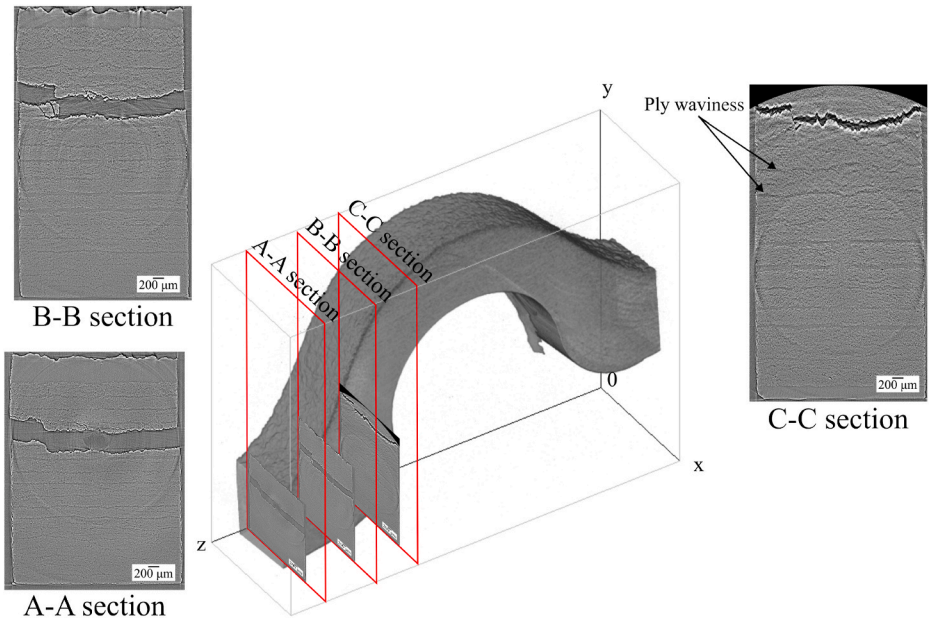

Fig. 10. SCT cross-sectional image at the location of failure; Section A-A showed inter-ply damage (out-of-plane delamination), Section B-B showed a combination between intra and inter-ply damages at the steepest slope region (highest shear). Section C-C showed a delamination propagation towards the centre of the part. (A colour version of this figure can be viewed online.)

outer surfaces of the sample in the transition corners. This phenomenon can be explained by considering a SCT image of the sample as shown in Fig. 8. These locations correspond to resin-rich regions (low fibre volume fraction) which resulted in insufficient carbon fibre diffraction to facilitate effective lattice parameter quantification. It should be noted that the SCT showed that there was no damage in this zone after failure. This result is perhaps surprising giving that these resin rich regions are typically weaker than areas that are fibre rich. However, these regions were far away from the areas of stress concentration, and therefore failure occurred before the resin-rich regions reached their nominal material strength.

3.2. Comparison of synchrotron study and numerical predictions

Although the quantification of the axial lattice strains from the fibres is relatively straightforward, the extraction of representative radial strains from the multi-scale framework was more challenging as the geometry and the resulting diffraction patterns were only representative of a selected region within the fibre. This situation is schematically illustrated in Fig. 11, in location (A) the graphite planes are nominally aligned with the incident beam and therefore constructive interference occurs and the {002} peak is observed on the detector. In contrast, at location (B) the graphite planes are perpendicular to the incident beam and no constructive interference occurs. The geometry of the HBB means that fibre bending will be induced and therefore the magnitude of the radial strain within the system will differ in the two regions. For this reason extraction of the radial strain within the appropriate region (A) is necessary to provide a direct comparison with the diffraction results. It is not immediately clear what percentage of the overall volume leads to constructive interference on the detector, as deviations from the scattering angle, $2\theta = 10.8°$ are detectable. However, stress equilibrium was used to determine that the average radial strain within the central 30% of the fibre was most representative of the sampled volume as shown in Fig. 11.

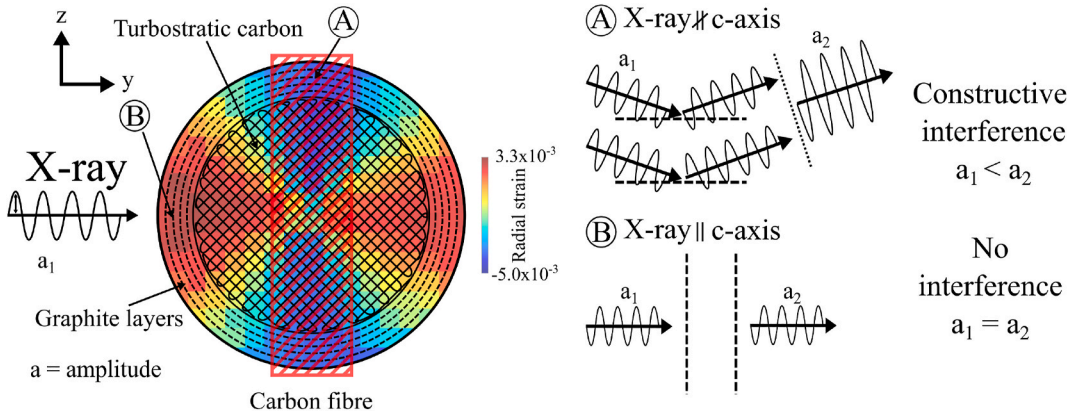

Fig. 11. Scattering and diffraction of incident X-rays on the {002} (radial) lattice spacing. When the direction of the incident beam is parallel to the atomic planes in (A) - constructive interference occurs. In contrast, when the incident beam is perpendicular to the atomic planes in (B) - no interference occurs. The region nominally leading to diffraction ($2\theta = 10.8°$) is the central 30% of the fibre cross-sectional area (red hatched box) and therefore radial strain averaging from the RVE is performed in this region for comparison with the experimental results. The fibre's longitudinal direction is along the x-axis. (A colour version of this figure can be viewed online.)

The two-dimensional lattice strain distribution between the SXRD experimental results and the meso-scale simulation are compared in Fig. 12 for both strain directions. It can be seen that the numerical FE results provided a good agreement with the experiment results in terms of load/strain trends and magnitudes. This demonstrates that the SXRD mapping technique is sensitive enough to reliably capture the strain variation within samples; the key goal of this approach. In addition, the SXRD goes further - it is also able to pick up the locations of strain concentration in the sample due to defects and localised effects that cannot be fully captured in a model. Such insights are crucial to extend existing understanding of CFRPs and the information provides an exciting and unique measurement of these effects.

To further compare the experimental results with the numerical simulation, a localised comparison between the two methods at the centre of the sample was made by averaging the through-thickness results from the inner ply to the outer ply, as shown in Fig. 13. The primary reason for selecting this location for the comparison was that it suffers least from the generation of defects (in contrast to the top and bottom) allowing a more representative comparison with the numerical validation to be made. It can be seen that the standard deviations (SD) of the SXRD radial strain were reasonably large, but the trends within the two profiles show a good match. As expected, the strain distribution from the model exhibits smooth trends. In contrast, the SXRD results show discontinuities which are associated with imperfections/defects within the sample. Differences between the two profiles are also expected from the boundary conditions which could not be perfectly fixed in the experiment.

The large confidence intervals in the SXRD results arise from the

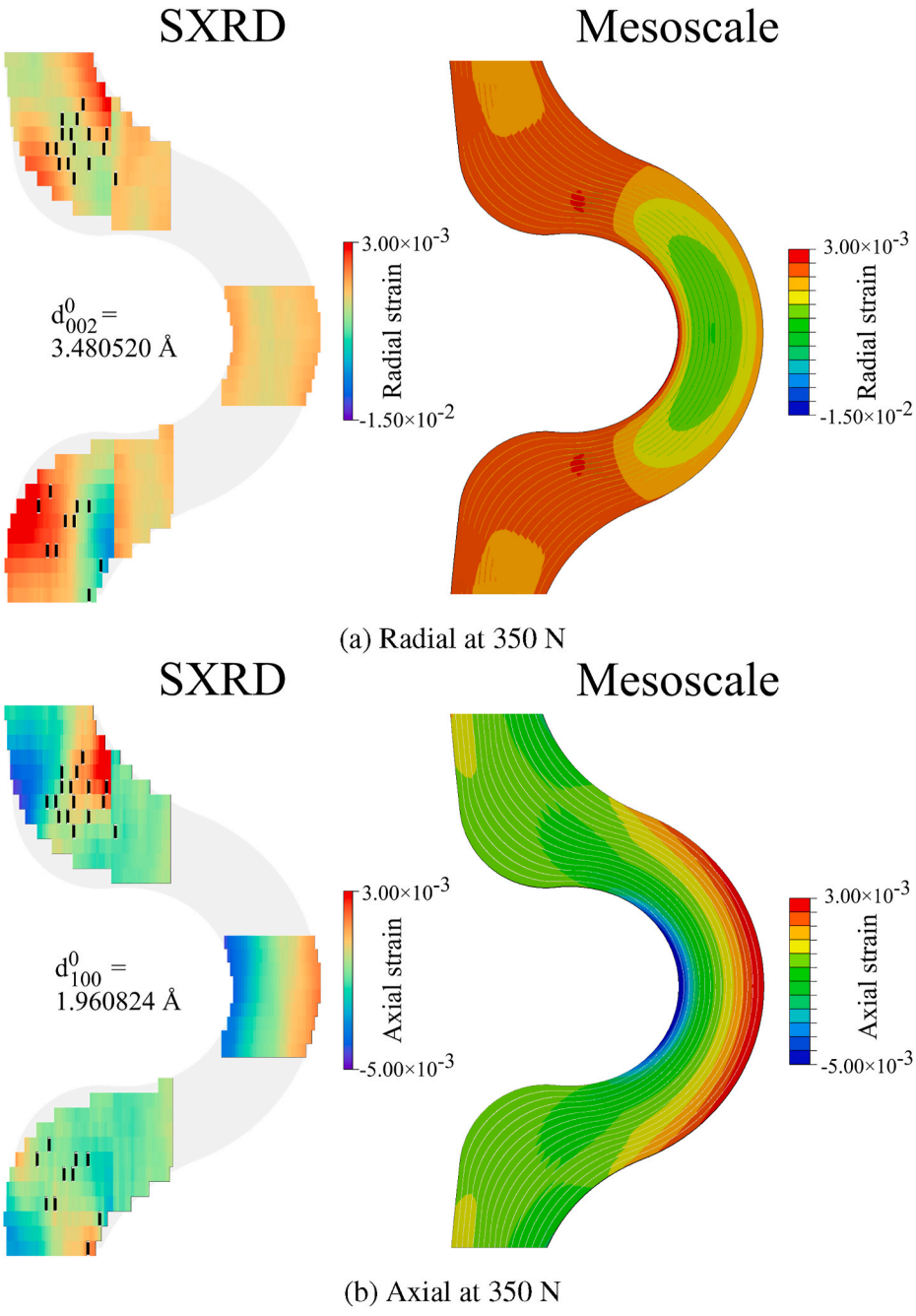

Fig. 12. Comparison between SXRD and mesoscale modelling simulation at (a) radial and (b) axial directions at 350 N in the elastic regime. (A colour version of this figure can be viewed online.)

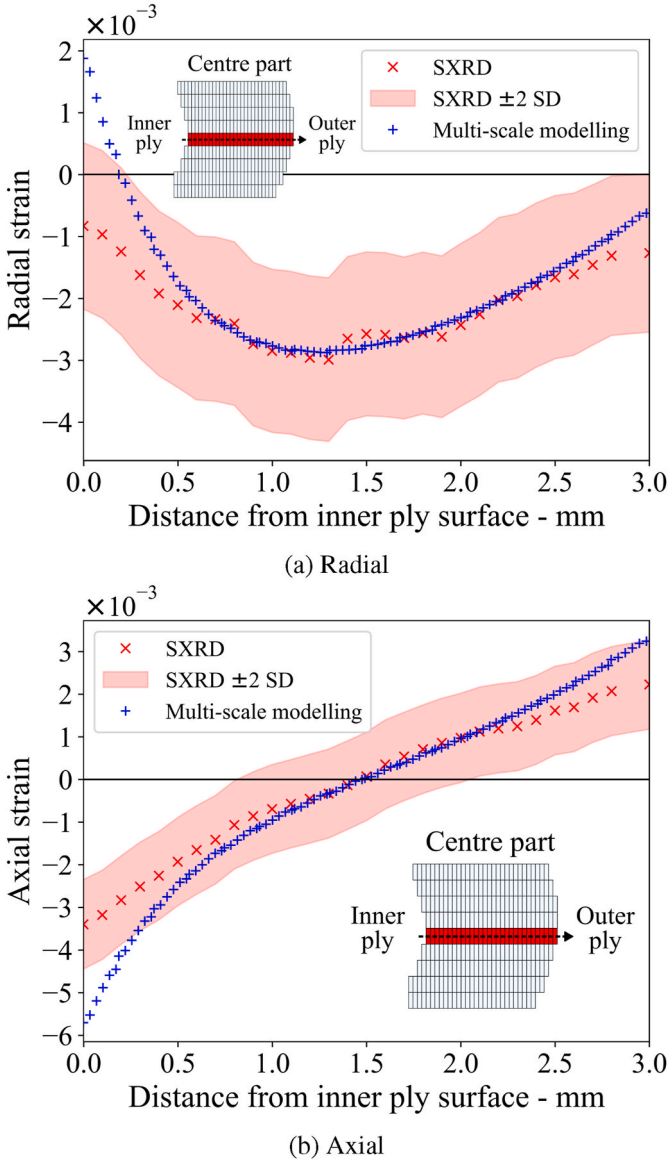

Fig. 13. SXRD (a) radial and (b) axial lattice strain as a function of distance from the inner to the outer surface (at the centre of the HBB); error contours represent ± two times the standard deviation from the mean strain. (A colour version of this figure can be viewed online.)

nature of the turbostratic carbon, which leads to a broad peak and somewhat reduced confidence in the peak centre fitting. A comparison between the confidence intervals in the axial and radial directions shows that the axial direction was found to be less affected by the semi-amorphous microstructure of the carbon. However, as outlined previously, this peak was more affected by shadows and low peak intensity. It should also be noted that the fibre strain comparison between two methods was much more straightforward in the axial direction as diffraction was the same over the entire fibre.

The biggest discrepancies between numerical and experimental results at the centre of the sample appear on the inner surface of the curvature for both fibre strain directions. These differences could originate from residual strains that are induced during the autoclave curing process. It is commonly known that residual strains in composite laminates can arise from the mismatch between the Coefficients of Thermal Expansions (CTEs) of the fibre and matrix and that they are present at the micro-scale during the cooling process [52]. This effect had been considered in the model with the temperature pre-defined field analysis, but discrepancies still exist. The exact origins of these differences not fully known but are likely to be induced by combined factors as outlined in more detail below.

To begin with, the discrepancies could be associated with the HBB geometry after curing. Volume fraction variations through the thickness are often observed in curved laminates, as was the case in this sample (Fig. 8). As highlighted by Wisnom et al. [53], the geometry across the varying radii results in a non-uniform ply thickness.This induces fibre bridging across the corner which increases the nominal radii when forming a laminate on a concave tool [54]. Corner thickening leads to a resin-rich zone and volume fraction variations which amplifies the spring-in effect [55]. This will influence the residual stress, particularly at the edges of the laminate.

In addition to the above, the surface closest to the tool (resin-rich layer) tends to have a higher CTE than the outer ply surface (resin-poor layer) resulting in geometry distortion and the development of non-uniform residual stress, even in a UD laminate [56]. Furthermore, residual stresses can arise during the curing due to differential strains between the part and tooling. These effects originate from the fact that the mould is typically manufactured from steel or aluminium (as in this experiment) which has a much higher CTE than the composite laminate. The inner ply surface, therefore, experiences a greater thermal expansion than the outer ply surface, resulting in a tensile stress gradient [57].

In summary, the forming geometry and tool-part interaction could induce a significant residual strain at the boundaries. Modelling these combined effects is a challenging problem which goes beyond the scope of this paper, but the location and expected trends in the experimental results (more tensile in the axial direction and more compressive in the radial) in comparison with the numerical results are observed. In order to analyse these effects further a composite tool could be used to minimise the dissimilarity in CTEs between the part and the tool.

Finally, a small asymmetric load distribution arising from the complex geometry of the HBB sample could have a significant impact on these discrepancies. Mazars et al. [58] was able to predict the location of damage effectively by taking the account of real boundary conditions evaluated from DVC to their FE model, which could not be achieved with the perfect boundary conditions. Future work will be needed to take this into consideration.

In order to assess the impact of these effects on failure mode, comparisons were drawn between the locations of delamination in the experiment and the numerical modelling. The five repeated loading tests showed nominally identical stiffnesses and a common failure location; single delamination was observed near the outer plies at the top part of the HBB as shown in the SCT image (Fig. 10). In contrast, the numerical simulation predicted single pure delamination near the centre of the sample on the inner surface of the curvature with a maximum failure load of 730 N which overestimated the structure strength by 38%. Given that this is the location where the numerical modelling could not reproduce the experimental result, it is perhaps unsurprising that this discrepancy occurred. However, the sophisticated models required to capture this tool-part interaction are beyond the scope of this project. The mean absolute percentage errors (MAPEs) between the SXRD results (actual value) and the numerical results (forecast value) were found to be 25.8% and 28.5% in radial and axial directions, respectively. This tool-part interaction could influence the through-thickness residual strain up to 3 plies away from the tool surface. By discarding these regions that this modelling did not account for, the MAPEs could be as low as 6.3% in radial and 22.4% in axial. The MAPE in the axial was still relatively high even without the edge discrepancies. It suggested that the imperfections within the structure could also significantly affect its behaviours. Further exploration into novel approaches to including these factors/imperfections in numerical modelling has the potential to reduce this discrepancy. These differences were deemed to be acceptably small to have shown the potential of the new experimental approach and to have enhanced the current understanding of the stress distribution in this sample.

4. Uncertainties, improvement and conclusion

4.1. SXRD for lattice strain measurement in CFRPs and uncertainties

The SXRD of the carbon fibre laminate has shown to have significant potential to be able to reliably quantify the lattice strain distribution of CFRPs. This offers the opportunity to substantially improve quantitative insights into the fibre microstructure for example during loading or in the quantification of residual stresses induced by the curing process. This method could also be used to study the localised behaviour of the fibres in CFRPs due to the existence of micro-defects such as voids, fibre kinking and wrinkles that dramatically reduce the material's strength. Unlike the DVC method which relies on the correlation between the movement of a feature within an investigated object; residual strains immediately after curing can be quantified. This approach also requires no modification to the CFRP (such as the addition of high contrast tracking nanoparticles) meaning that the samples truly representative of in-service conditions can be studied. The implications of this approach are significant - it will increase current confidence in the material properties used during modelling and will help to accelerate the industrial shift from experimental coupon testing towards the more cost effective use of reliable virtual testing. As an added advantage, this method can quantify fibre orientation in multi-directional laminates as well as characterising ply misalignment which has important implications for strength and stiffness in industrial applications. The outcomes of this new approach are therefore primarily new/complementary information which can be used alongside existing NDT techniques to further explore the material behaviour at unprecedented level.

It should be noted that these types of experiments have only recently become viable due to the advancement of two fields. Firstly, significant improvements in SXRD detectors are beginning the reliable quantification of amorphous diffraction patterns for the first time [59]. Secondly, advances in the multi-scale modelling of carbon fibre composites have facilitated the quantification of fibre strains within a composite structure in a rapid and reliable manner. The micro-scale model used in this study has been necessary to separate the strains in the fibre phase out from the matrix phase. It should be noted that this study is amongst the first to experimentally validate the results of such a composite model at the microscopic level which is a challenging task by other means.

4.2. Future improvement

Despite the benefits of this approach, the uncertainties/confidence bounds of the SXRD results are still relatively significant as shown by the uncertainty contours in Fig. 13. The errors and uncertainties of this SXRD technique have been propagated throughout the post-processing pipeline to provide reliable estimates of these values. However, ultimately this method cannot overcome the complexity of the microstructure within carbon fibres which significantly impacts the precision of the results that can be obtained. This leads to a broadening of diffraction spots which are challenging to reliably fit and is also influenced by scattering and shadowing of the sample from the incident radiation beam. In addition, this experiment suffered from the influence of diffraction and scattering arising from the glassy carbon load cell itself. As a result, it was impossible to reliably fit the {110} reflections (which correspond to the fibre hoop strain). For this reason, several key improvements to the method have been identified and a subsequent experiment implementing these changes is being prepared:

- To design a new load cell system in which the incident and diffracted beam does not interact with any supporting structures. This should significantly reduce the background scattering.
- Apply guard slits to the focused beam in order to reduce shadowing effects on the detector.
- Extend the exposure times in to increase peak intensity and reduce the impact of noise on the diffraction peaks.
- Reduce the sample to detector distance to ~80 mm in order to capture the {002}, {100} and {110} lattice peaks, or use another X-ray diffraction detector with a larger detection area. This will help facilitate simultaneous quantification of strain in all directions.
- Apply resin blocks at sample ends to improve general compliance to the experimental loading conditions and prevent fibre blooming, which is common in a UD composite laminate subjected to compressive end loads.
- Modify the in-house grips to facilitte loading via the resin blocks

These new improvements are expected to increase the accuracy of the SXRD results and reduce the uncertainties arising from peak fitting. It is believed that this will reduce the error of the measurements to an acceptable level, such that it can be used regularly for the characterisation of CFRP composites.

4.3. Conclusion

In this study, SXRD has been shown to facilitate the quantification of fibre orientation and lattice strain distributions within a composite laminate structure for the first time. These through-thickness strains are essential in enhancing the existing understanding of delamination failure and cannot be easily measured by established strain quantification methods at the micro-scale resolution required. During this process, fibre orientations are simultaneously identified via the rotation of the {002} lattice plane. By comparing the changes in the microstructure within the carbon fibres at different load increments, the evolution of strain maps around features of interest is revealed. The SXRD results showed good agreement with numerical simulations extracted from the multi-scale modelling of the fibres to facilitate the quantification of fibre strains in the radial and axial directions at unprecedented resolution. The MAPEs between the experiment and this modelling prediction were determined to be 25.8% and 28.5% for radial and axial directions, respectively.

The main discrepancies between the experimental results and numerical model were on the inner surface due to the addition of residual strains induced from the non-uniform thermal history arising from forming geometry and tool-part interaction that constrained the fibres after the consolidation. Modifications to the sample and the experimental setup will be used in future to prevent fibre blooming and minimise noise during the data acquisition, respectively.

This approach has significant potential to enhance current understanding of load-bearing in CFRP materials and systems, with important implications for improving current knowledge of load redistribution and the impact of defects at an unprecedented resolution. Such insights are crucial to continue to expand the use of this promising material class and reduce the reliance on excessive safety factors in industrial applications. The potential to further optimise understanding of the micro-scale effects that can dominate macro-scale stiffness and failure is necessary for driving towards virtual multi-scale testing that is required by industry. This paper provides not only the fundamental basis on which this improved understanding can be developed, but also highlights new and promising routes to optimise and refine the presented approach in future.

CRediT authorship contribution statement

Jiraphant Srisuriyachot: Data curation, Formal analysis, Validation, Visualization, Writing – original draft. **Sophie A.M. McNair:** Methodology, Investigation. **Yang Chen:** Software. **Thomas Barthelay:** Investigation. **Rob Gray:** Investigation. **Jean Bénézech:** Supervision, Writing – review & editing. **Igor P. Dolbnya:** Supervision, Writing – review & editing. **Richard Butler:** Supervision, Conceptualization, Funding acquisition, Methodology, Writing – review & editing. **Alexander J.G. Lunt:** Conceptualization, Supervision, Methodology, Writing – original draft, Writing – review & editing.

Declaration of competing interest

The authors declare that they have no known competing financial interests or personal relationships that could have appeared to influence the work reported in this paper.

Acknowledgements

This work was supported by the UKRI - Engineering and Physical Sciences Research Council Grant 'Certification for Design - Reshaping the Testing Pyramid' EP/S017038/1. Richard Butler holds the Royal Academy of Engineering - GKN Aerospace Research Chair. Jiraphant Srisuriyachot is funded by this chair. Diamond Light Source is acknowledged for providing the beamtime on B16 beamline under the experiment number MM23372-1.

References

[1] T. Luke, Through-thickness Compression Testing and Theory of Carbon Fibre Composite Materials, Ph.D. thesis, University of Manchester, 2011.
[2] S. Lee, E. Jo, W. Ji, Digital volume correlation technique for characterizing subsurface deformation behavior of a laminated composite, Compos. B Eng. 194 (2020), 108052.
[3] M. Mehdikhani, C. Breite, Y. Swolfs, J. Soete, M. Wevers, S.V. Lomov, L. Gorbatikh, Digital volume correlation for meso/micro in-situ damage analysis in carbon fiber reinforced composites, Compos. Sci. Technol. 213 (2021), 108944.
[4] R. Brault, A. Germaneau, J.-C. Dupré, P. Doumalin, S. Mistou, M. Fazzini, In-situ analysis of laminated composite materials by x-ray micro-computed tomography and digital volume correlation, Exp. Mech. 53 (7) (2013) 1143–1151.
[5] E. Schöberl, C. Breite, A. Melnikov, Y. Swolfs, M. Mavrogordato, I. Sinclair, S. Spearing, Fibre-direction strain measurement in a composite ply under quasi-static tensile loading using digital volume correlation and in situ synchrotron radiation computed tomography, Compos. Appl. Sci. Manuf. 137 (2020), 105935.
[6] E. Schöberl, C. Breite, S. Rosini, Y. Swolfs, M. Mavrogordato, I. Sinclair, S. M. Spearing, A novel particle-filled carbon-fibre reinforced polymer model composite tailored for the application of digital volume correlation and computed tomography, J. Compos. Mater. 55 (14) (2021) 1907–1934.
[7] M. Folomeshkin, Y.V. Pisarevsky, P. Prosekov, Y. Volkovsky, A. Kumskov, Y. Grigoriev, E. Ligacheva, A. Targonskii, A. Blagov, M. Kovalchuk, X-ray diffraction analysis and electron microscopy of the carbon fiber structure, Crystallogr. Rep. 64 (1) (2019) 1–5.
[8] I.M. Djordjević, D.R. Sekulić, M.N. Mitrić, M.M. Stevanović, Non-Hookean elastic behavior and crystallite orientation in carbon fibers, J. Compos. Mater. 44 (14) (2010) 1717–1727.
[9] J. Wang, N. Salim, B. Fox, N. Stanford, Anisotropic compressive behaviour of turbostratic graphite in carbon fibre, Appl. Mater. Today 9 (2017) 196–203.
[10] M.J. Behr, B.G. Landes, B.E. Barton, M.T. Bernius, G.F. Billovits, E.J. Hukkanen, J. T. Patton, W. Wang, C. Wood, D.T. Keane, et al., Structure-property model for polyethylene-derived carbon fiber, Carbon 107 (2016) 525–535.
[11] W. Hoffman, W. Hurley, P. Liu, T. Owens, The surface topography of non-shear treated pitch and PAN carbon fibers as viewed by the STM, J. Mater. Res. 6 (8) (1991) 1685–1694.
[12] A.G. Dumanlı, A.H. Windle, Carbon fibres from cellulosic precursors: a review, J. Mater. Sci. 47 (10) (2012) 4236–4250.
[13] D. Johnson, Structure-property relationships in carbon fibres, J. Phys. Appl. Phys. 20 (3) (1987) 286.
[14] C. Eichenseer, I. Wittmann, C. Hartig, G.A. Schneider, N. Schell, W. Hintze, In situ measurement of lattice strains in mixed ceramic cutting tools under thermal and mechanical loads using synchrotron radiation, Prod. Eng. 7 (2–3) (2013) 283–289.
[15] N. Baimpas, A.J. Lunt, I.P. Dolbnya, J. Dluhos, A.M. Korsunsky, Nano-scale mapping of lattice strain and orientation inside carbon core sic fibres by synchrotron x-ray diffraction, Carbon 79 (2014) 85–92.
[16] A. Lunt, M. Xie, N. Baimpas, S. Zhang, S. Kabra, J. Kelleher, T. Neo, A. Korsunsky, Calculations of single crystal elastic constants for yttria partially stabilised zirconia from powder diffraction data, J. Appl. Phys. 116 (5) (2014), 053509.
[17] D. Collins, M. Mostafavi, R. Todd, T. Connolley, A. Wilkinson, A synchrotron X-ray diffraction study of in situ biaxial deformation, Acta Mater. 90 (2015) 46–58.
[18] T. Nishino, H. Naito, K. Nakamura, K. Nakamae, X-ray diffraction studies on the stress transfer of transversely loaded carbon fibre reinforced composite, Compos. Appl. Sci. Manuf. 31 (11) (2000) 1225–1230.
[19] T. Nishino, D. Hirokane, K. Nakamae, X-ray diffraction studies of the environmental deterioration of a transversely loaded carbon-fibre-reinforced composite, Compos. Sci. Technol. 61 (16) (2001) 2455–2459.
[20] M.R. Wisnom, M. Jones, Delamination due to interaction between curvature induced interlaminar tension and stresses at terminating plies, Compos. Struct. 32 (1–4) (1995) 615–620.
[21] S. Mespoulet, Through-thickness Test Methods for Laminated Composite Materials, Ph.D. thesis, the University of London, 1998.
[22] K. Kedward, R. Wilson, S. McLean, Flexure of simply curved composite shapes, Composites 20 (6) (1989) 527–536.
[23] T. Nguyen, Effects of Curvature on the Stresses of a Curved Laminated Beams Subjected to Bending, Ph.D. thesis, The Faculty of the Graduate School of the University of Texas at Arlington, 2010.
[24] W. Jackson, R. Martín, An Interlaminar Tensile Strength Specimen, ASTM International.
[25] P. A. Lagace, D. B. Weems, A Through-The-Thickness Strength Specimen for Composites, ASTM International.
[26] M. R. Wisnom, M. Jones, A comparison between interlaminar and in-plane shear strength of unidirectional glass fibre-epoxy, Adv. Compos. Lett. 3 (2).
[27] J.-H. Kim, K.-H. Nguyen, J.-H. Choi, J.-H. Kweon, Experimental and finite element analysis of curved composite structures with C-section, Compos. Struct. 140 (2016) 106–117.
[28] M.R. Wisnom, 3-D finite element analysis of curved beams in bending, J. Compos. Mater. 30 (11) (1996) 1178–1190.
[29] H. Zhang, T. Sui, E. Salvati, D. Daisenberger, A.J.G. Lunt, K.S. Fong, X. Song, A. M. Korsunsky, Digital image correlation of 2D X-ray powder diffraction data for lattice strain evaluation, Materials 11 (3) (2018) 427.
[30] J. Filik, A. Ashton, P. Chang, P. Chater, S. Day, M. Drakopoulos, M. Gerring, M. Hart, O. Magdysyuk, S. Michalik, et al., Processing two-dimensional x-ray diffraction and small-angle scattering data in dawn 2, J. Appl. Crystallogr. 50 (3) (2017) 959–966.
[31] ABAQUS, Analysis User's Manual, Version 6.14, Dassault Systemes Simulia, Inc.
[32] O. Falcó, R. Ávila, B. Tijs, C. Lopes, Modelling and simulation methodology for unidirectional composite laminates in a virtual test lab framework, Compos. Struct. 190 (2018) 137–159.
[33] B. Schäfer, D. Dörr, L. Kärger, Reduced-integrated 8-node hexahedral solid-shell element for the macroscopic forming simulation of continuous fibre-reinforced polymers, Procedia Manuf. 47 (2020) 134–139, 23rd International Conference on Material Forming.
[34] T.A. Fletcher, T. Kim, T.J. Dodwell, R. Butler, R. Scheichl, R. Newley, Resin treatment of free edges to aid certification of through thickness laminate strength, Compos. Struct. 146 (2016) 26–33.
[35] W. Cui, M. Wisnom, M. Jones, A comparison of failure criteria to predict delamination of unidirectional glass/epoxy specimens waisted through the thickness, Composites 23 (3) (1992) 158–166.
[36] C.G. Dávila, E.R. Johnson, Analysis of delamination initiation in postbuckled dropped-ply laminates, AIAA J. 31 (4) (1993) 721–727.
[37] P. Camanho, F. Matthews, Delamination onset prediction in mechanically fastened joints in composite laminates, J. Compos. Mater. 33 (10) (1999) 906–927.
[38] H. Hu, F. Niu, T. Dou, H. Zhang, Rehabilitation effect evaluation of cfrp-lined prestressed concrete cylinder pipe under combined loads using numerical simulation, Math. Probl Eng. (2018), 3268962.
[39] M. Benzeggagh, M. Kenane, Measurement of mixed-mode delamination fracture toughness of unidirectional glass/epoxy composites with mixed-mode bending apparatus, Compos. Sci. Technol. 56 (4) (1996) 439–449.
[40] A. Puck, H. Schürmann, Failure Analysis of FRP Laminates by Means of Physically Based Phenomenological Models, The World-Wide Failure Exercise, 2004, pp. 832–876.
[41] L. Yang, Y. Yan, Z. Ran, Y. Liu, A new method for generating random fibre distributions for fibre reinforced composites, Compos. Sci. Technol. 76 (2013) 14–20.
[42] Z. Hu, R. Karki, Prediction of mechanical properties of three-dimensional fabric composites reinforced by transversely isotropic carbon fibers, J. Compos. Mater. 49 (12) (2015) 1513–1524.
[43] L. Mishnaevsky, P. Brøndsted, Micromechanical modeling of damage and fracture of unidirectional fiber reinforced composites: a review, Comput. Mater. Sci. 44 (4) (2009) 1351–1359.
[44] F. Naya Montáns, Prediction of Mechanical Properties of Unidirectional FRP Plies at Different Environmental Conditions by Means of Computational Micromechanics, Ph.D. thesis, Universidad Politécnica de Madrid, 2017.
[45] L. Gélébart, J. Derouillat, et al., AMITEX FFTP, URL, https://amitexfftp.github.io/AMITEX/general/index.html. (Accessed 10 May 2022).
[46] Y. Chen, L. Gélébart, C. Chateau, M. Bornert, C. Sauder, A. King, Analysis of the damage initiation in a SiC/SiC composite tube from a direct comparison between large-scale numerical simulation and synchrotron X-ray micro-computed tomography, Int. J. Solid Struct. 161 (2019) 111–126.
[47] M. Endo, 'Carbon fiber', in: High-performance and Specialty Fibers: Concepts, Technology and Modern Applications of Man-Made Fibers for the Future, The Society of Fiber Science and Technology, Japan.
[48] E. Frank, L.M. Steudle, D. Ingildeev, J.M. Spörl, M.R. Buchmeiser, Carbon fibers: precursor systems, processing, structure, and properties, Angew. Chem. Int. Ed. 53 (21) (2014) 5262–5298.
[49] D. Jang, M.E. Lee, J. Choi, S.Y. Cho, S. Lee, Strategies for the production of pan-based carbon fibers with high tensile strength, Carbon 186 (2022) 644–677.
[50] X. Qian, J. Zhi, L. Chen, J. Zhong, X. Wang, Y. Zhang, S. Song, Evolution of microstructure and electrical property in the conversion of high strength carbon fiber to high modulus and ultrahigh modulus carbon fiber, Compos. Appl. Sci. Manuf. 112 (2018) 111–118.
[51] A. Galiguzov, A. Malakho, V. Kulakov, A. Kenigfest, E. Kramarenko, V. Avdeev, The influence of carbon fiber heat treatment temperature on carbon-carbon brakes characteristics, Carbon Lett. 14 (1) (2013) 22–26.
[52] L. Yang, Z. Wu, Y. Cao, Y. Yan, Micromechanical modelling and simulation of unidirectional fibre-reinforced composite under shear loading, J. Reinforc. Plast. Compos. 34 (1) (2015) 72–83.

[53] M. Wisnom, M. Jones, G. Hill, Interlaminar tensile strength of carbon fibre-epoxy–specimen size, layup and manufacturing effects, Adv. Compos. Lett. 10 (4) (2001) 171–177.
[54] P. Hubert, A. Poursartip, Aspects of the compaction of composite angle laminates: an experimental investigation, J. Compos. Mater. 35 (1) (2001) 2–26.
[55] M. Wisnom, M. Gigliotti, N. Ersoy, M. Campbell, K. Potter, Mechanisms generating residual stresses and distortion during manufacture of polymer–matrix composite structures, Compos. Appl. Sci. Manuf. 37 (4) (2006) 522–529.
[56] D.W. Radford, Cure shrinkage induced warpage in flat uni-axial composites, J. Compos. Technol. Res. 15 (4) (1993) 290–296.
[57] G. Twigg, A. Poursartip, G. Fernlund, Tool–part interaction in composites processing. part i: experimental investigation and analytical model, Compos. Appl. Sci. Manuf. 35 (1) (2004) 121–133.
[58] V. Mazars, O. Caty, G. Couégnat, A. Bouterf, S. Roux, S. Denneulin, J. Pailhès, G. L. Vignoles, Damage investigation and modeling of 3D woven ceramic matrix composites from x-ray tomography in-situ tensile tests, Acta Mater. 140 (2017) 130–139.
[59] A.J. Lunt, P. Chater, A. Kleppe, N. Baimpas, T.K. Neo, A.M. Korsunsky, Residual strain mapping through pair distribution function analysis of the porcelain veneer within a yttria partially stabilised zirconia dental prosthesis, Dent. Mater. 35 (2) (2019) 257–269.